Letters

Multimodal Split-Bus Boost-LLC Resonant Converter

Yuezhao Sun, Xiaogao Xie, *Senior Member, IEEE*, and Hanjing Dong

***Abstract*—This article proposes a multimodal split-bus boost-LLC resonant converter suitable for wide-range applications. In the proposed topology, the bus of the conventional full-bridge LLC resonant converter is split. Specifically, the bus of the first half-bridge arm is directly connected to the input voltage source, while the bus of the second half-bridge arm is boosted by an integrated boost circuit formed by the boost inductor connected to the input voltage source and the second bridge arm. A fixed-frequency duty cycle control is applied to the second switching bridge arm to raise its bus voltage, thereby adjusting the equivalent input voltage of the resonant tank and modifying the voltage gain of the converter. In addition, through topological reconfiguration, the primary-side inverter bridge can transition from full-bridge mode to half-bridge mode, enabling the converter to achieve a fourfold voltage gain range. Finally, a 1-kW laboratory prototype with 400 V input and 200–800 V output voltage was developed. Experimental results show that the prototype achieved 97.5% peak efficiency under full-bridge LLC mode, which increased to 97.8% when operating in half-bridge LLC mode. The efficiency remained above 96.2% within the whole output voltage range under the rated output current.**

***Index Terms*—LLC resonant converter, split bus, wide voltage gain.**

I. Introduction

LLC has become the preferred topology for the poststage converter due to its soft-switching characteristics and electromagnetic interference suppression capability [1]. However, traditional full-bridge LLC resonant converter still faces challenges, such as its limited output gain range [2].

To overcome these challenges and achieve wide output range for LLC converters, researchers have proposed many solutions [3], [4], [5], [6], [7].

The first type of solutions is to adopt new modulation strategies besides conventional pulse frequency modulation (PFM). For example, the hybrid modulation strategy composed of PFM and phase-shift modulation is applied to the full-bridge LLC converter [3]. Although the voltage gain has been expanded, the lagging half-bridge arm loses zero voltage swiching (ZVS) when the phase-shift angle is too large.

Received 30 July 2025; revised 2 October 2025; accepted 13 October 2025. Date of publication 15 October 2025; date of current version 23 December 2025. This work was supported by the National Natural Science Foundation of China under Grant 52177174. *(Corresponding author: Xiaogao Xie.)*

The authors are with the School of Automation, Hangzhou Dianzi University, Hangzhou 310018, China (e-mail: xiexg@hdu.edu.cn).

Color versions of one or more figures in this article are available at https://doi.org/10.1109/TPEL.2025.3622146.

Digital Object Identifier 10.1109/TPEL.2025.3622146

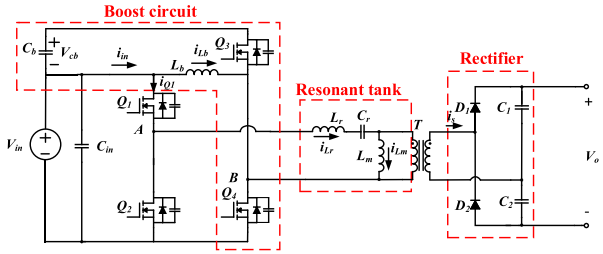

Fig. 1. Split-bus *boost*-LLC resonant converter: Mode I: $D_{Q1} = 0.5$ *and* $D_{Q2} = \overline{D}_{Q1}$; $D_{Q4} = D$ *and* $D_{Q3} = \overline{D}_{Q4}$ Duty cycle control; Mode II: D_{Q1}= 0.5 and $D_{Q2} = \overline{D}_{Q1}$; D_{Q4}= *0* and D_{Q3}= *1* PFM control.

Another type of solutions is adjusting the parameters resonant components. In [4], the controllable switching inductance is used, and similarly, Gao et al. [5] introduced the controllable switching capacitance strategy. However, additional devices will bring more loss and higher volume.

The last type is structural reconfiguration, including primary topology reconfiguration and secondary rectifier reconfiguration. For example, a reconfigurable bridge arm consisting of five switches is used to implement four operating modes through different switching combinations [6], enabling a fourfold adjustable gain range with relatively high overall efficiency. In [7], by controlling the turn-ON and turn-OFF of the auxiliary switch, the rectifier can be switched between full-bridge rectification and voltage doubling rectification, so that a wider voltage gain range can be obtained. For those reconfigurable topologies, a relatively complex control strategy is needed to achieve continuous voltage gain. In [8], a morphing control was applied to a reconfigurable LLC converter, which makes the LLC converter enter dual full-bridge, hybrid full-bridge, half bridge, and dual half-bridge operation modes. In [9], by splitting the resonant branch, parallel operation of two half-bridges and a combined full-bridge and half-bridge configuration can be achieved, resulting in a 2.5-fold gain variation range. In [10], by reorganizing two active switches, the rectifier can be reconfigured as a full-bridge rectifier, a hybrid voltage-multiplier rectifier, and a voltage-multiplier rectifier, which makes the converter achieve three times the voltage gain adjustment.

In response to the current state of research, a split-bus boost-*LLC* resonant converter is proposed in this article, as shown in Fig. 1. In this topology, the bus of the full-bridge LLC resonant converter is split. By applying fixed-frequency duty cycle control to the second half-bridge arm, the corresponding bus voltage

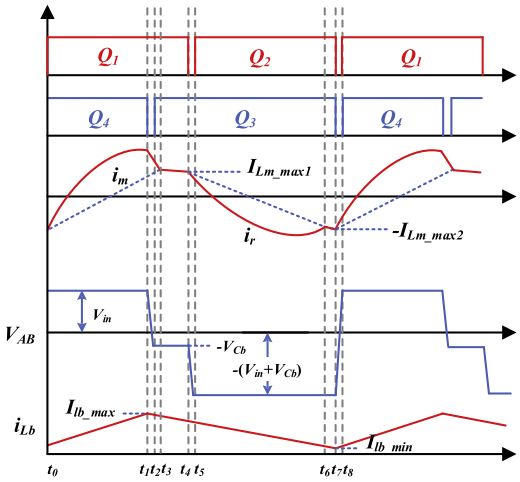

Fig. 2. Waveform of the converter operating in Mode I.

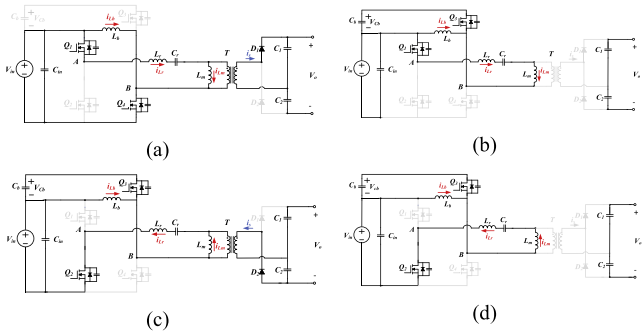

Fig. 3. Equivalent circuits of the converter during different steady-state operating stages in Mode I. (a) Steady-state stage I. (b) Steady-state stage II. (c) Steady-state stage III. (d) Steady-state stage IV.

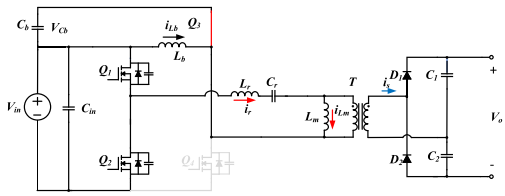

Fig. 4. Equivalent circuits of the converter operating in Mode II.

TABLE I
R_e AND Q VALUES UNDER DIFFERENT OUTPUT VOLTAGES IN MODE II

V_o	$0.75V_{nom}$	V_{nom}	$1.5V_{nom}$
R_e	$\frac{3n^2}{2\pi^2}\frac{V_{nom}}{I_{\max}}$	$\frac{2n^2}{\pi^2}\frac{V_{nom}}{I_{\max}}$	$\frac{3n^2}{\pi^2}\frac{V_{nom}}{I_{\max}}$
Q	$\frac{4}{3}Q_{nom}$	Q_{nom}	$\frac{2}{3}Q_{nom}$

can be adjusted, thereby regulating the equivalent input voltage of the resonant tank and modifying the voltage gain of the converter. Furthermore, through topological reconfiguration, the primary-side inverter bridge can be switched from full-bridge mode to half-bridge mode, allowing the converter to achieve over fourfold voltage gain range.

II. Operating Mode of the Proposed Converter

As shown in Fig. 1, the proposed split-bus boost-LLC resonant converter is composed of an integrated boost circuit and an LLC resonant converter, where D_{Q1}–D_{Q4} represent the duty cycles of Q_1–Q_4, and $\overline{D}_{Q1} = 1 - D_{Q1}$ and $\overline{D}_{Q3} = 1 - D_{Q4}$. The switching arm consisting of Q_1 and Q_2 is referred to as the first switching bridge arm, while the switching arm consisting of Q_3 and Q_4 is referred as the second switching bridge arm. The integrated boost circuit is composed of the boost inductor L_b and the second switch bridge arm, which can increase the input voltage of this bridge arm, thereby achieving the voltage boost of the resonant tank and reducing the resonant tank current. The resonant circuit comprises the resonant inductance L_r, the resonant capacitance C_r, and the magnetizing inductance L_m of the transformer. Under the fixed-frequency operating mode, the output voltage gain range can be adjusted by varying the duty cycle of the second switching bridge arm. In addition, by modifying the control strategy of Q_3 and Q_4, the topology can be switched from full-bridge LLC mode (Mode I) to half-bridge LLC mode (Mode II), which further expands the voltage gain range of the circuit.

The key steady-state waveforms under Mode I are shown in Fig. 2. There exist four main steady-state operation stages. The equivalent circuits corresponding to these stages are illustrated in Fig. 3 .

Steady-state stage I [t_0–t_1]: During this stage, Q_1 and Q_4 are ON while Q_2 and Q_3 are OFF. The resonant tank voltage V_{AB} is equal to the input voltage V_{in}. The voltage across the boost inductor is equal to the input voltage, and the boost inductor current i_{Lb} increases linearly. Simultaneously, diode D_1 conducts, the voltage across the transformer is clamped by the voltage of capacitor C_1 and the magnetizing current i_{Lm} increases linearly. At the same time, resonance occurs between the resonant inductor L_r and the resonant capacitor C_r. The equivalent circuit of this stage is shown in Fig. 3(a).

Steady-state stage II [t_3–t_4]: During this stage, Q_1 and Q_3 are ON while Q_2 and Q_4 are OFF. On the secondary side, both D_1 and D_2 are OFF. The voltage-doubling capacitors C_1 and C_2 supply energy to the load. The resonant tank voltage V_{AB} and the voltage across the boost inductor are both equal to $-V_{Cb}$. The boost inductor current i_{Lb} to decreases linearly. Resonance occurs between L_r, L_m, and C_r. The equivalent circuit of this stage is shown in Fig. 3(b).

Steady-state stage III [t_5–t_6]: During this stage, Q_2 and Q_3 are ON while Q_1 and Q_4 are OFF. On the secondary side, D_2 conducts. The resonant tank voltage V_{AB} is equal to -(V_{in} +V_{Cb}). L_r and C_r resonates, while the boost inductor current i_{Lb} continues to decrease linearly by $-V_{cb}$. The equivalent circuit of this stage is shown in Fig. 3(c).

Steady-state stage IV [t_6–t_7]: During this stage, the states of the switches are as same as that in stage III. On the secondary side, the rectifiers are OFF. i_{Lb} continues to decrease, while L_r, L_m, and C_r resonate. The equivalent circuit of this stage is shown in Fig. 3(d).

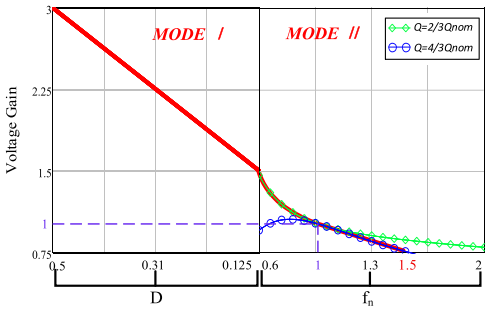

Fig. 5. Combined gain curve of the converter.

When Q_3 is always ON while Q_4 is always OFF, the converter operates as a half-bridge LLC (see Mode II), as shown in Fig. 4. The conventional PFM control is utilized to regulate the voltage gain. L_b is connected in parallel with C_b. Since the capacitive reactance of C_b is much lower than the inductive reactance of L_b, almost no current flows through L_b.

III. Voltage Gain Analysis and Design Considerations

A. Gain Analysis

In Mode I, during a single switching period, the volt–second balance relationship indicates that

$$V_{Cb} = V_{\text{in}} D/(1-D) \tag{1}$$

where D is the duty cycle of Q_4. From the analysis of the above operating modes and the voltage values at each stage, the fundamental component of the equivalent input voltage V_{AB} can be obtained with Fourier decomposition

$$V_{AB1} = \frac{4}{\pi} \cdot (2D+0.5) V_{\text{in}} \sin(2\pi f_s t). \tag{2}$$

Similarly, the fundamental component of the equivalent output voltage V_{oe} can be obtained

$$V_{oe1} = \frac{4}{\pi} \cdot \frac{1}{2} n V_o \sin(2\pi f_s t) \tag{3}$$

where n is the transformer turns ratio and f_s is the switching frequency. When the converter operates at the resonant point in Mode I, the voltage gain of the converter can be expressed as

$$G_1(D) = \frac{nV_o}{2V_{\text{in}}} = 2D + 0.5. \tag{4}$$

The voltage gain G_2 of the converter in Mode II is the same as that of a conventional half-bridge LLC resonant converter. Table I presents a comparison of the characteristics at different output voltages under the maximum output current $I_{\max}$ in Mode II, including the ranges of equivalent resistance R_e and quality factor Q. Here, V_{nom} denotes the output voltage at the resonant point, and Q_{nom} refers to the quality factor corresponding to V_{nom} and the maximum output current $I_{\max}$,$Q_{nom} = \sqrt{L_r/C_r}/R_{enom}$ and $R_{enom} = 2n^2 V_{nom}/\pi^2 I_{\max}$.

Thereafter, the combined gain curve can be plotted out, as shown in Fig. 5. The gain range in Mode I is [1.5, 3] and the corresponding duty cycle range is [0.125, 0.5]. Under Mode II, Q varies from 2/3 Q_{nom} to 4/3 Q_{nom} and the gain range varies from 1.5 to 0.75. Correspondingly, the normalized frequency f_n varies from 0.6 to 1.5.

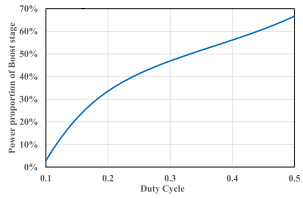

Fig. 6. Relationship curve of the power ratio of the boost converter versus D under rated output current.

B. Power Allocation

In Mode I, the duty cycle determines the power distribution. In Fig. 2, based on the different resonant states, this interval can be divided into five stages. The time-domain expressions of the resonant tank current i_r during each stage are as follows:

$$i_r(t) = \begin{cases} I_{rP}\sin(\omega_s t + \theta_{P0}) & t_0 < t < t_1 \\ I_{rE}\sin(\omega_s t - \omega_s t_1 + \theta_{E0}) & t_1 < t < t_3 \\ I_{rO}\sin(\frac{\omega_s t - \omega_s t_3}{\sqrt{1+k}} + \theta_{O0}) & t_3 < t < t_5 \\ I_{rN}\sin(\omega_s t - \omega_s t_5 + \theta_{N0}) & t_5 < t < t_6 \\ I_{rO2}\sin(\frac{\omega_s t - \omega_s t_6}{\sqrt{1+k}} + \theta_{O20}) & t_6 < t < t_8 \end{cases} \tag{5}$$

where I_{rP}, I_{rE}, I_{rO}, I_{rN}, and I_{rO2} and θ_{P0}, θ_{E0}, θ_{O0},θ_{N0}, and θ_{O20} represent the peak current values and the initial phase angles in each stage and $k = L_m/L_r$, $t_0 = 0$, $t_1 = DT_S$, $t_5 = T_s/2$, and $t_8 = T_s$. The unknown variables can be determined by applying the continuity conditions of the resonant tank inductor current and the capacitor voltage.

The input current i_{in} divides into the currents flowing through Q_1 and the current flowing through the boost inductor L_b, i.e., $i_{\text{in}} = i_{Q\ 1} + i_{Lb}$. The average boost inductor current, which is denoted as $I_{Lb\cdot\text{avg}}$, can be expressed as

$$I_{Lb\_\text{avg}} = I_{in} - \frac{1}{T_s}\int_0^{\frac{T_s}{2}} i_r(t)dt. \tag{6}$$

The ratio of the boost converter to the total power is

$$\frac{P_{\text{Boost}}}{P_{\text{in}}} = \frac{V_{\text{in}}\left(I_{\text{in}} - \frac{1}{T_s}\int_0^{\frac{T_s}{2}} i_r(t)dt\right)}{V_{\text{in}} I_{\text{in}}}. \tag{7}$$

With numerical calculation method, the relationship curve of the power ratio of the boost converter versus D under rated output current can be obtained, as shown in Fig. 6.

C. Soft-switching Condition

It is easy to know that the ZVS condition for Q_1 and Q_2 is identical to that in conventional LLC resonant converter; hence, it will not be discussed here. As shown in Fig. 2, Q_4 turns OFF at time t_1. After that, the sum of i_r and i_{Lb} charges the output capacitance of Q_4 and discharges the output capacitance of Q_3. Hence, Q_3 is easy to achieve ZVS. At time t_7, Q_3 turns OFF. To ensure ZVS of Q_4, inequality (8) should be satisfied

$$I_{Lm\_\max 2} - I_{Lb\_\min} \geq I_{\text{ZVS}} \tag{8}$$

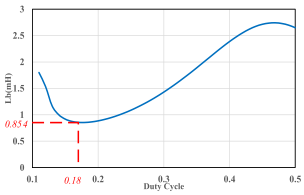

Fig. 7. Relationship curve of L_{b_cri} versus D under rated output current.

where $I_{Lm\_\max\ 2}$ is the negative peak value of i_{Lm}, $I_{Lb\_\min}$ is the minimum value of i_{Lb}, and I_{ZVS} is the minimum current required for realizing ZVS for Q_4

$$I_{\mathrm{ZVS}} = \frac{2C_{oss}V_{\mathrm{in}}}{t_d(1-D)} \tag{9}$$

$$I_{Lb\_\min} = I_{Lb\_\mathrm{avg}} - \frac{DV_{\mathrm{in}}}{2L_b}T_s \tag{10}$$

where C_{oss} is the output capacitance of Q_4 and t_d is the dead time between the driving signals of Q_3 and Q_4.

Inequality (11) is obtained by combining (8) and (10), which gives the critical inductance of L_b for achieving ZVS of Q_4.

$$L_b \le \frac{DV_{\mathrm{in}}T_s}{2(I_{\mathrm{ZVS}} + I_{Lb\_avg} - I_{Lm\_\max 2})} \tag{11}$$

where $-I_{Lm\_\max\ 2} = i_r(t_0)$, and I_{Lb_avg} can be obtained according to (6). Thereafter, the relationship curve of the critical inductance of L_{b_cri} versus D can be obtained with numerical calculation, as shown in Fig. 7. The minimum value of L_{b_cri} on the curve is the optimal inductance of L_b that can achieve ZVS of Q_4 over the whole output voltage range and load range.

D. Duty Cycle Limitation

The voltages across Q_1 and Q_2 equal V_{in}; hence, 650 V commercial silicon carbide (SiC) MOSFET can be utilized. The voltages across Q_3 and Q_4 equal the sum of the input voltage V_{in} and the capacitor voltage V_{Cb}. According to (1), the voltages across Q_3 and Q_4 are related to D. Therefore, higher duty cycle means higher voltage stress on Q_3 and Q_4. Considering the voltage stress, $D_{\max}$ should be lower than 0.6 so that 1200 V commercial SiC MOSFET can be applied with 200 V voltage margin. Besides, Fig. 6 shows that the power ratio of the boost converter increases as duty cycle D increases, which means larger size of boost inductor as $D_{\max}$ increases. Therefore, $D_{\max}$<0.5 is a relatively optimal choice.

IV. Experimental Result

Based on the above analysis and design considerations, a laboratory prototype with a rated power of 1 kW has been developed. Table II details the key parameters and components of the converter, and Fig. 8 shows the photograph of the prototype.

Fig. 9 illustrates the steady-state waveforms of the converter operating in Mode I under different output voltages. i_{Lr} represents the resonant tank current, while $v_{gs\cdot Q4}$ and $v_{ds\cdot Q4}$ denote the gate drive signal and the drain–source voltage of the primary-side switch Q_4. In Fig. 9(a), the converter operates with rated power of 1 kW. It can be seen that Q_4 conducts with a duty cycle of 0.5, and $v_{ds\cdot Q4}$ drops to zero before the arrival of $v_{gs\cdot Q4}$, enabling ZVS for Q_4. In Fig. 9(b) and (c), the duty cycles of switch Q_4 are 0.31 and 0.125, respectively, which are generally consistent with the gain analysis discussed. In both cases, ZVS is successfully achieved for Q_4. Compared to Fig. 9(a), the load in Fig. 9(d) is lighter, resulting in a decrease in the resonant tank current. Consequently, Q_4 can achieve ZVS more easily due to the reduced load.

Fig. 10 shows the steady-state waveforms of the converter operating in Mode II under various output voltages. $v_{gs\cdot Q2}$ and $v_{ds\cdot Q2}$ denote the gate drive signal and the drain–source voltage of Q_2. It can be observed that ZVS is achieved for switch Q_2 over the whole output voltage range. The switching frequency varies from 60.5 to 152.1 kHz, which closely aligns with the theoretical analysis.

Fig. 11 shows the experimental waveforms of mode shift. The controller monitors whether the output voltage reaches the critical switching point to initiate a change in operating mode.

TABLE II
Components Parameters of the Experimental Prototype

V_{in}	400 V	L_r	100 μH
C_{in}	470 μF	C_r	25.3 nF
L_b	850 μH	L_m	485 μH
C_b	1 μF	C_1/ C_2	230 μF
Q_1 and Q_2	IV1Q06060T3G (INVENTCHIP, 650V/60mΩ)	Q_3 and Q_4	IV1Q12080T3 (INVENTCHIP, 1200V/80mΩ)
V_o/I_o	200~800 V/0.5~1.25 A	f_s	60~160 kHz

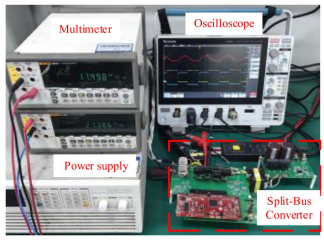

Fig. 8. Photograph of the 1-kW laboratory prototype.

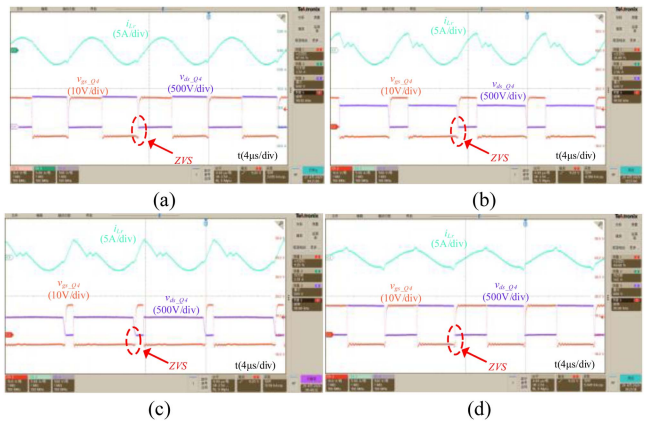

Fig. 9. Steady-state waveforms of the converter operating in Mode I. (a) V_o= 800V and I_o= 1.25 A. (b)V_o= 600 V and I_o= 1.25 A. (c)V_o= 400 V and I_o= 1.25 A. (d) V_o= 800 V and I_o= 0.5 A.

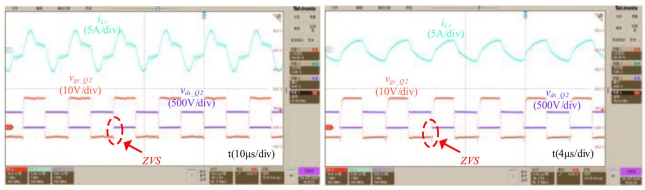

(a) (b)

Fig. 10. Steady-state waveforms of the converter operating in Mode II. (a) V_o= 400 V and I_o= 1.25 A. (b) V_o = 200 V and I_o = 1.25 A.

TABLE III
COMPARISON OF TOPOLOGIES FOR WIDE VOLTAGE RANGE

Schemes	H5-LLC [6]	TM-LLC [8]	SP-LLC [9]	RHV-LLC [10]	This work
Modulation scheme	PFM	PFM	PFM	PWM+ PFM	PWM+ PFM
Number of magnetic components	4	4	3	3	3
Number of switches	5	6	4	6	4
Number of diodes	4	4	4	4	2
Voltage range	100–420 V (output)	45–135 V (input)	80–200 V (input)	150–450 V (output)	200–800 V (output)
Power level	1.1 kW	230 W	1 kW	3.3 kW	1 kW
Peak efficiency	97.6%	95.5%	97.5%	97%	97.8%
Resonant frequency	50–150 kHz	88–133 kHz	80–160 kHz	150–250 kHz	60–160 kHz

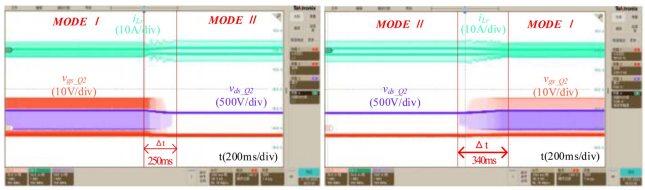

(a) (b)

Fig. 11. Experimental waveforms of mode switching. (a) Switching from Mode I to Mode II. (b) Switching from Mode II to Mode I.

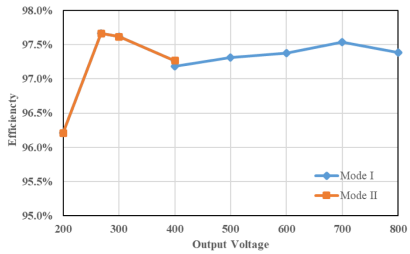

Fig. 12. Test efficiency curves of the prototype over the whole output voltage range with I_o = 1.25 A.

The transition is achieved by gradually adjusting the duty cycle of Q_4. In Fig. 11(a), the duty cycle of Q_4 decreases from 0.12 to 0 while it increases in the opposite direction in Fig. 11(b). The transitions are completed in 250 and 340 ms, respectively, and the resonant tank current remains stable in both cases.

Fig. 12 presents the overall efficiency curve of the converter with rated output current. Under Mode I, the peak efficiency of 97.5% is achieved when the output voltage V_o is 700 V. Under Mode II, the peak efficiency reaches 97.8% at V_o = 268 V, where the converter operates at the resonant point. When the output voltage drops to 200 V, the converter operates in an overresonant state in Mode II, which leads to increased switching losses due to the higher operating frequency. As a result, the efficiency slightly decreases but still reaches 96.2%.

A comparison among the proposed topology and some recently reported topologies for wide voltage range applications is shown in Table III. It is evident that the proposed solution achieves a broader gain range while using the minimum number of magnetic components and semiconductor devices. Furthermore, the efficiency performance of the prototype is also superior to other topologies. In summary, the proposed topology features the fewest components count, wide voltage range, and good efficiency.

V. CONCLUSION

This article presents a novel multimodal split-bus LLC resonant converter designed for electric vehicle charging stations operating over a wide voltage range. By controlling the switching states of the power transistors, the converter can be shifted between two distinct operating modes, enabling a broader gain range while maintaining high efficiency. To validate the feasibility of the proposed approach, a 1-kW laboratory prototype with 400 V input and 200–800 V output was developed. Experimental results confirm that the proposed converter features wide voltage gain range and high efficiency.

REFERENCES

[1] J. Wu, S. Li, S. Tan, and Y. Hui, "Frequency folding for LLC resonant converters in EV charging applications," *IEEE Trans. Power Electron.*, vol. 38, no. 4, pp. 5041–5054, Apr. 2023.

[2] H. Yu, X. Xie, and H. Dong, "Phase-Shift Modulated Hybrid LLC and half-bridge converter with fixed frequency for wide voltage gain range application," *IEEE Trans. Power Electron.*, vol. 39, no. 1, pp. 717–732, Jan. 2024.

[3] U. Mumtahina and P. J. Wolfs, "Multimode optimization of the phase-shifted LLC series resonant converter," *IEEE Trans. Power Electron.*, vol. 33, no. 12, pp. 10478–10489, Dec. 2018.

[4] Y. Wei, Q. Luo, X. Du, N. Altin, and A. Mantooth, "Analysis and design of the LLC resonant converter with variable inductor control based on time-domain Analysis," *IEEE Trans. Ind. Electron.*, vol. 67, no. 7, pp. 5432–5443, Jul. 2019.

[5] L. Gao et al., "Variable-gain LLC converter with series–Parallel hybrid switch-controlled capacitor network," *IEEE Trans. Power Electron.*, vol. 40, no. 3, pp. 3885–3898, Nov. 2024.

[6] C. Li, H. Wang, and M. Shang, "A five-switch bridge based reconfigurable LLC converter for deeply depleted PEV charging applications," *IEEE Trans. Power Electron.*, vol. 34, no. 5, pp. 4031–4035, May 2019.

[7] L. Costa, G. Buticchi, and M. Liserre, "A fault-tolerant series-resonant DC–DC Converter," *IEEE Trans. Power Electron.*, vol. 32, no. 2, pp. 900–905, Feb. 2017.

[8] Y. Wei, Q. Luo, and H. Alan Mantooth, "A novel LLC converter with topology morphing control for wide input voltage range application," *IEEE J. Emerg. Sel. Topics Power Electron.*, vol. 10, no. 2, pp. 1563–1574, Apr. 2022.

[9] W. Sun, Y. Xing, H. Wu, and J. Ding, "Modified high-efficiency LLC converters with two split resonant branches for wide input-voltage range applications," *IEEE Trans. Power Electron.*, vol. 33, no. 9, pp. 7867–7879, Sep. 2018.

[10] X. Tang, Y. Xing, H. Wu, and J. Zhao, "An improved LLC resonant converter with reconfigurable hybrid voltage multiplier and PWM-plus-PFM hybrid control for wide output range applications," *IEEE Trans. Power Electron.*, vol. 35, no. 1, pp. 185–197, Jan. 2020.